Nuclear Engineering and Technology 55 (2023) 3140–3149

Contents lists available at ScienceDirect

Nuclear Engineering and Technology

journal homepage: www.elsevier.com/locate/net

Original Article

Tackling range uncertainty in proton therapy: Development and evaluation of a new multi-slit prompt-gamma camera (MSPGC) system

Youngmo Ku [a], Sehoon Choi [a], Jaeho Cho [a], Sehyun Jang [a], Jong Hwi Jeong [b], Sung Hun Kim [b], Sungkoo Cho [c], Chan Hyeong Kim [a, *]

[a] Depaprtment of Nuclear Engineering, Hanyang University, Seoul, 04763, Republic of Korea
[b] Proton Therapy Center, National Cancer Center, Goyang-si, Gyeonggi-do, 10408, Republic of Korea
[c] Department of Radiation Oncology, Samsung Medical Center, Sungkyunkwan University School of Medicine, Seoul, 06351, Republic of Korea

ARTICLE INFO

Article history:
Received 18 April 2023
Received in revised form
17 May 2023
Accepted 22 May 2023
Available online 12 July 2023

Keywords:
Proton therapy
Range uncertainty
Multi-slit prompt-gamma camera
Range measurement
Range verification

ABSTRACT

In theory, the sharp dose falloff at the distal end of a proton beam allows for high conformal dose to the target. However, conformity has not been fully achieved in practice, primarily due to beam range uncertainty, which is approximately 4% and varies slightly across institutions. To address this issue, we developed a new range verification system prototype: a multi-slit prompt-gamma camera (MSPGC). This system features high prompt-gamma detection sensitivity, an advanced range estimation algorithm, and a precise camera positioning system. We evaluated the range measurement precision of the prototype for single spot beams with varying energies, proton quantities, and positions, as well as for spot-scanning proton beams in a simulated SSPT treatment using a phantom. Our results demonstrated high accuracy (<0.4 mm) in range measurement for the tested beam energies and positions. Measurement precision increased significantly with the number of protons, achieving 1% precision with 5×10^8 protons. For spot-scanning proton beams, the prototype ensured more than 5×10^8 protons per spot with a 7 mm or larger spot aggregation, achieving 1% range measurement precision. Based on these findings, we anticipate that the clinical application of the new prototype will reduce range uncertainty (currently approximately 4%) to 1% or less.

1. Introduction

In the field of radiotherapy, the sharp dose falloff of the proton beam at the distal beam end (i.e., the beam range) theoretically allows for highly conformal dose delivery to the target [1]. However, this conformity is not fully utilized in clinical practice, primarily due to range uncertainty caused by inaccuracies in photon-derived tissue stopping power, inter-fractional anatomical changes, and patient setup errors [2]. To ensure target coverage and sparing of organs at risk (OARs), a safety margin is added to the beam range in treatment planning for robustness against range uncertainty [3–7]. Additionally, to avoid the risk of range under-/over-shoot, the lateral beam edge is often used instead of the much sharper distal beam edge for sparing adjacent OARs [8]. These approaches, however, result in less conformal dose distribution (i.e., deposition of substantial dose to the surrounding normal tissue) and a lower degree of freedom in beam arrangement (i.e., avoidance of beam direction toward a neighboring OAR) than potentially achievable [9]. This implies that there is an opportunity for improvement by reducing range uncertainty. Tattenberg et al. [9] reported the possibility of reducing normal tissue complication probability (NTCP) for neighboring OARs even with a slight reduction of range uncertainty, i.e., from the current level of 4%–3%.

To reduce range uncertainty in proton therapy, many researchers have investigated in vivo range verification techniques based on prompt-gamma imaging (PGI) [10]. This technique, suggested by Stichelbaut and Jongen [11] and experimentally demonstrated by Min et al. [12], is considered the most promising approach due to the high correlation between the depth-dose distribution and prompt-gamma (PG) emission profile and its capability for real-time range monitoring [13]. Various PGI systems have been proposed and experimentally evaluated, including the

* Corresponding author.
E-mail address: chkim@hanyang.ac.kr (C.H. Kim).

https://doi.org/10.1016/j.net.2023.05.028

knife-edge slit camera [14–16], the multi-slit prompt-gamma camera (MSPGC) [17], gamma electron vertex imaging (GEVI) system [18–22], and Compton cameras [23–28], but none are commercially available yet.

The first PGI system clinically applied is the knife-edge slit camera [29], which is the most studied in this field. Its main advantage is the high detection efficiency compared to other systems, which is crucial considering that most PGI systems suffer from low detection efficiency and resultant high statistical uncertainties in measured beam range, especially for spot-scanning proton therapy (SSPT) [30]. However, the falloff in the measured PG distribution at the distal beam end is not sharp, and the measured distribution is dependent on the spot beam position and patient geometry, which makes measuring the beam range based solely on the PG measurement difficult [30,31]. For this reason, the knife-edge camera measures the proton-beam range by comparing the measured PG distribution with a reference PG distribution generated by an analytical or Monte Carlo simulation [31,32]. Consequently, the accuracy of range measurement with this approach highly depends on the accuracy of the simulation, which is prone to errors when a complex geometry, such as human anatomy, is involved.

In our previous work, we developed a prototype multi-slit prompt-gamma camera (MSPGC), another PGI system [17]. Multiple experiments with the prototype for clinical proton beams confirmed that it can directly measure the proton beam range without referring to an analytical or Monte Carlo simulation. Additionally, the prototype exhibited a much sharper falloff in the measured PG distribution at the beam end. However, the precision of the prototype in range measurement was not sufficient to reduce range uncertainty due to limitations in PG detection sensitivity and the curve-fitting-based range estimation algorithm [17]. Furthermore, the prototype lacked its own positioning system, making it difficult to apply to different clinical cases. Meanwhile, significant efforts have been made to improve range measurement by developing a powerful range estimation algorithm [33], which provides significantly higher precision in range estimation than the existing range estimation algorithm.

In the present study, a new MSPGC prototype was developed for clinical application in SSPT, aiming to overcome the limitations of the previous prototype by primarily improving PG detection sensitivity, adopting a powerful range estimation algorithm, and incorporating a newly developed precision camera positioning system. The performance of the new prototype was compared with that of the previous prototype by analyzing their PG distributions measured for clinical proton beams under identical conditions. Moreover, the range measurement precision of the new MSPGC was evaluated for clinical proton beams of different beam energies, proton quantities, and beam positions. Lastly, the range measurement precision of the MSPGC was assessed in an SSPT treatment for a phantom following a typical treatment procedure.

2. Materials and methods

2.1. New multi-slit prompt-gamma camera (MSPGC)

2.1.1. Collimator, detectors, and front-end signal processing

Fig. 1 shows the head of the new MSPGC prototype developed in the present study. A parallel multi-slit collimator, which comprises a total of 72 slits (W 3 × H 100 × D 100 mm^3) in two rows (i.e., 36 slits for each row) in a staggered layout, is placed in front of the scintillator array. The septal slab (W 3 × H 105 × D 100 mm^3) and the frame of the collimator are made of tungsten and stainless steel, respectively. Behind each slit, two CsI(Tl) scintillators (W 4 × H 50 × D 70 mm^3, Hangzhou Yong Hee Photonics Co., Hangzhou, China) are positioned to detect PGs passing through the slit. Each scintillator is optically coupled with a Si PIN photodiode (S3588-08, Hamamatsu Photonics KK, Japan) using optical cement (BC-600, Saint-Gobain Crystals, France), and its entire surface was wrapped with reflective film (Enhanced Specular Reflector, 3 M, MN) except for the coupling surface. The collimator and the scintillator array feature high mechanical precision (i.e., <0.1 mm), which ensures the geometrical precision of the PG distribution acquired by the camera. In addition, to assemble the collimator and detector array with very high mechanical precision, a side straight positioning block of 0.01 mm positioning precision (TSSB30-8, Misumi, Japan) is placed on the four junctional sides. Compared with the previous prototype [17], the field of view (FOV) of PG detection was expanded 1.5 times (i.e., from 144 mm to 216 mm), by increasing the width of the slit and the thickness of the septal slab from 2 to 3 mm. In addition, the length of the scintillator was increased from 30 to 70 mm to increase PG detection efficiency.

At the rear of the scintillator array, the front-end signal processing system is positioned, which converts the output signal from each detector (i.e., scintillator coupled with a photodiode) into a Gaussian pulse using a charge sensitive preamplifier (CR-110, Cremat Inc., MA) and a shaping amplifier (shaping time = 1.2 μs). The output signal of the front-end signal processing system is transmitted via a multi-channel coaxial cable to the data acquisition (DAQ) system, which will be described in Section 2.1.3.

2.1.2. Camera positioning system

Fig. 2 shows the camera positioning system developed in the present study for precise and automatic positioning of the camera relative to the patient in the treatment room. The positioning system enables movement of the camera head in six degrees of freedom (DOF): linear translation in three orthogonal directions (i.e., x, y, and z) and rotation in three Euler angles (i.e., yaw, pitch, and roll). The vertical motion (in the z direction) is controlled by a scissor-type lift with a linear actuator (TA23, TiMOTION, Taiwan). The other motions (i.e., x, y, yaw, pitch, and roll) are controlled by a five DOF motion stage installed on the lift with high-precision servo motors (Ezi-SERVO-ST-60L-A-PN50, Fastech, Republic of Korea).

The precision position tracking device (PPT; WorldViz, CA) employed in the positioning system measures the real-time position of the camera in the treatment room with very high accuracy (<0.5 mm). The PPT consists of PPT markers, which emit infrared rays to indicate their positions, and PPT sensors to locate the markers in the treatment room. The PPT markers are placed near the eight vertices of the camera head, and three PPT sensors are installed in the treatment room. Using the measured PPT marker positions, the position and direction of the camera head are determined with rigid body analysis.

Based on the motion control system and PPT, the camera automatically and precisely moves to the imaging position using feedback loop control, according to the following procedure: (1) the magnitudes of translations and rotations for the camera to reach the imaging position are calculated; (2) the position and direction of the camera are controlled by the actuator and motors according to the calculated magnitudes; (3) if the difference between the current and the imaging position is less than the predefined threshold (0.5 mm, 0.5°), the arrangement procedure is completed; otherwise, steps (1–3) are repeated from the current position. For the safety of the patient and operator, the maximum speed of translation and rotation is limited to 1 cm/s and 3°/s, and the camera moves only while the enable button on the positioning system is pressed by the operator. Even though the speed is limited, the entire camera arrangement procedure requires less than 1 min with several feedback loops, thereby delaying treatment only minimally.

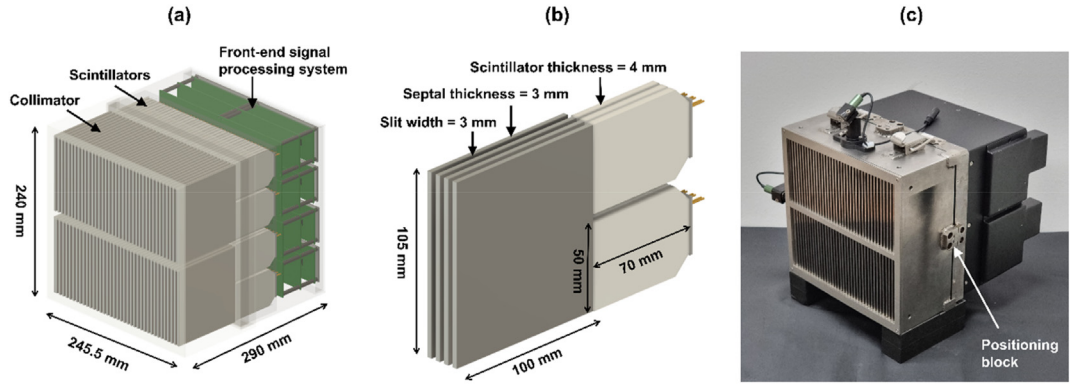

Fig. 1. Multi-slit prompt-gamma camera (MSPGC) prototype developed in present study: schematic of (a) camera head and (b) array of septal slabs and scintillators (only for three slits as an example), with (c) photograph of camera head.

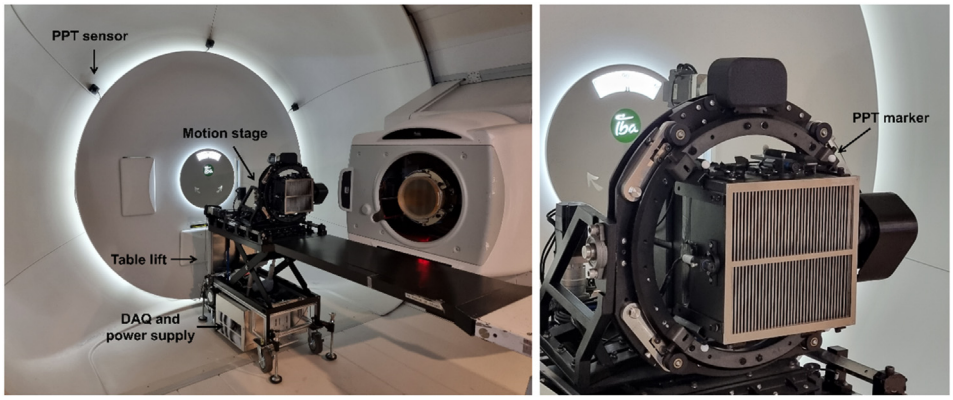

Fig. 2. Positioning system of new multi-slit prompt-gamma camera (MSPGC).

2.1.3. Data acquisition (DAQ) system

The data acquisition (DAQ) system of the MSPGC consists of eight slave boards and one master board. The slave board comprises (1) 18 analog-to-digital converters (ADCs; AD9251BCPZ-40, Analog Devices, MA, USA) with 14-bit resolution for digitizing individual detector signals from the camera head and (2) a field-programmable gate array (FPGA; Arria V 5AGXMA5G4F31C5G, Intel, CA, USA) for calculating the height and timing of a digitized pulse signal. The master board consists of (1) an FPGA (Cyclone V 5CEBA7F31C7N, Intel, CA, USA) for collecting the pulse data from the slave boards and (2) a universal serial bus (USB) 3.0 module (EZ-USB FX3, Infineon Technologies, Germany) for transferring the pulse data to a personal computer. Multi-channel coaxial cables (HHSC-1-07-300-SU-SU, Samtec, IN, USA) are used for data transmission from the slave boards to the master board.

During the operation of the MSPGC, ADCs individually digitize corresponding detector signals at the speed of 40 mega samples per second. Simultaneously, the signals are continuously smoothed using a moving average method with a 200 ns window to reduce high-frequency noise. Note that the window is much shorter than the pulse shaping time (1200 ns), thereby limiting the loss of energy (pulse height) resolution by over-smoothing. When the signal exceeds a predefined threshold level (approximately 200 keV) in a DAQ channel, the measurement of pulse height and timing is triggered, assuming that an energy deposition event occurred in the corresponding scintillator. The pulse height is determined as the maximum height of the signal before the signal falls below the threshold level, and the pulse timing is considered to be the zero-crossing time of the constant fraction discriminator [34]. The pulse height and timing data obtained in the DAQ channel in the slave board are then immediately transferred to the master board. The master board collects data from the eight slave boards and transfers them to a personal computer via the universal serial bus module.

2.2. Performance evaluation of camera

The performance of the new MSPGC prototype was evaluated using clinical proton beams at the proton therapy facility (Proteus 235, IBA, Belgium) of the National Cancer Center (NCC) in Korea. Fig. 3 shows an illustration explaining the experimental setups in the present study. Note that the precision of the new prototype was evaluated as 1.5 times the standard deviation in range measurement for a fair comparison with range uncertainty, which is generally expressed as 1.5 times the standard deviation of beam range.

Before acquiring the PG distributions, energy calibration was performed to convert the pulse height recorded in the DAQ to the energy deposited in the scintillator. For the calibration, the pulse height spectra of ^{22}Na (57.0 μCi) and ^{137}Cs (80.0 μCi) check sources were acquired in turn by 144 detector channels, and linear fitting was performed for each detector channel using the 511, 662, and 1275 keV peaks in the energy spectra. The energy calibration process is mostly automated, and the entire energy calibration took less than 5 min, including the time to acquire the energy spectra (i.e., 2 min for each check source).

In this study, the range estimation algorithm recently developed by Ku et al. [33] was used to estimate the beam range from the

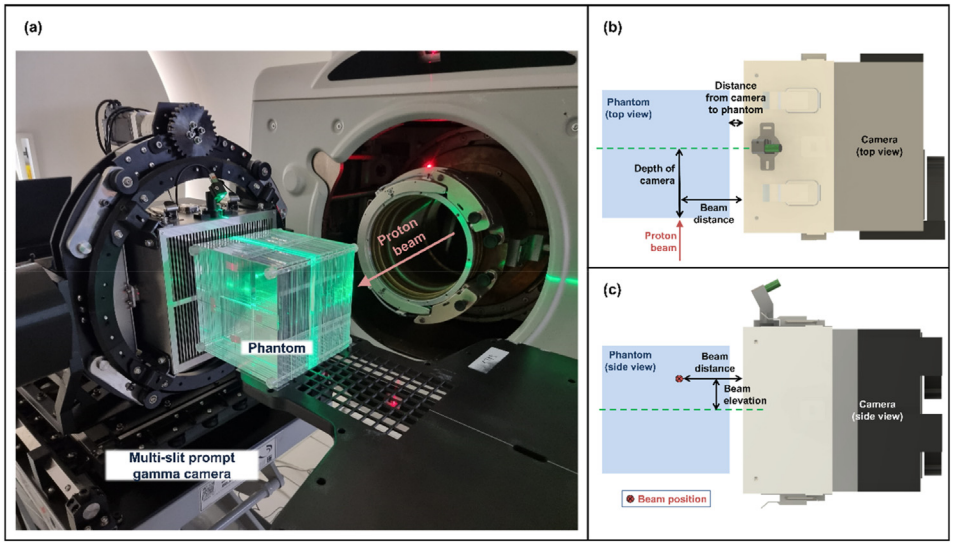

Fig. 3. (a) Experimental setup for proton-beam-range measurement using multi-slit prompt-gamma camera (MSPGC) prototype and schematic diagram of (b) top and (c) side view of experimental setup.

acquired PG distribution. This new algorithm locates the centroid of the falloff in the PG distribution, providing significantly higher precision than the curve-fitting-based range estimation algorithm adopted by the previous prototype [17,35]. More information on the range estimation algorithm can be found in [33].

2.2.1. Comparison with previous prototype

The performances of the new and previous prototypes were compared using their PG distributions, acquired under identical conditions. For this, a solid phantom (W 30 × H 30 × D 30 cm^3), which is a stack of 30 solid plate phantoms (W 30 × H 30 × D 1 cm^3; SP34, IBA, Germany), was irradiated by a 95.09 MeV spot beam. The number of protons was 8.73 × 10^9. The beam distance and the distance from the camera to the phantom were set to 200 and 100 mm, respectively (see Fig. 3). The depth of the camera was 70 mm, and the beam elevation was 0 mm. The relative qualities of PG distributions acquired by the new and previous prototypes were compared using the peak count (as a relative measure of efficiency), signal-to-noise ratio (SNR), and figure of merit (FOM), as devised in [36]. The acquisitions of PG distributions were repeated ten times for each prototype.

2.2.2. Range measurement for single spot beam

The accuracy and precision of the new prototype in beam-range measurement were evaluated for different spot beam conditions using a polymethyl methacrylate (PMMA) phantom (W 180 × H 180 × D 180 mm^3). First, PG distributions were acquired by the new prototype for different beam energies, proton quantities (i.e., the number of protons per beam), and beam positions. The beam energy ranged from 99.68 to 159.78 MeV, equivalent to the true ranges of 62.2–153.6 mm in the phantom. The number of protons per spot varied from 2 × 10^7 to 5 × 10^9. The beam position was varied in terms of two variables: beam distance (50–150 mm) and beam elevation (0–75 mm). Then, the range estimation algorithm [33] was applied to determine the range of the spot beam from the acquired PG distribution. The range measurement was repeated 10–100 times depending on the experimental conditions, in order to evaluate the precision in range measurement. In all cases, unless otherwise noted, the beam distance and the distance from the camera to the phantom were 100 and 10 mm, respectively, the depth of the camera was 70 mm, and the beam elevation was 0 mm.

2.2.3. Range measurement for spot-scanning proton beam

To evaluate the feasibility of the new prototype for clinical application, SSPT treatment plans were generated for a clinical target volume (CTV) of spherical shape with a 25 mm radius in the PMMA phantom by a commercial proton treatment planning system (TPS, Eclipse, v8.12). For the treatment planning, the phantom was scanned with a slice thickness of 1 mm using a computed tomography (CT) scanner (Siemens Sensation Open CT scanner, Siemens Medical Solutions USA, Inc., Malvern, PA). A known relative linear stopping power of PMMA, 1.16 [37], was assigned uniformly throughout the phantom to exclude uncertainty in converting CT number to proton stopping power. The center of the CTV was located at 100 mm depth in the phantom in the beam direction and at the center of the lateral cross section of the phantom. The considered prescription doses were 1 and 2 Gy, representing the doses in a field per fraction for conventional proton therapy, i.e., a 60 Gy total prescription dose in 30 fractions with one or two fields. The generated treatment plan contained 11 energy layers (104.8–137.8 MeV) in both 1 and 2 Gy prescription dose cases.

During the irradiation of the spot-scanning proton beam, the new prototype acquired the PG distribution for each spot beam individually. The depth of the camera was 90 mm, and the distance from the camera to the phantom was 10 mm. The vertical center of the camera was aligned at the center of the CTV.

To reduce the Poisson noise, the PG distribution of each spot was merged with those of the neighboring spots by 3D Gaussian spot aggregation [15,39,40]. In this process, the PG distribution of the aggregation spot was replaced by the sum PG distribution of neighboring spots (including the aggregation spot itself) weighted by a Gaussian function. The weight for a neighboring spot was determined by the following equation:

$$w = \begin{cases} e^{-\frac{1}{2}\left(\frac{d}{\sigma}\right)^2} & \text{if } d \le 3\sigma \\ 0 & \text{otherwise} \end{cases}$$

where w is the weight, d is the distance of the neighboring spot from the aggregation spot, and σ is the aggregation parameter. Note that only the spots at a distance of 3 σ or less from the aggregation

spot were considered as a neighboring spot. During the aggregation, the PG distribution of the neighboring spot was shifted in the longitudinal direction by the gap between the planned ranges of the neighboring and aggregation spots.

The aggregation parameter should be determined considering the degradation of the spatial resolution of the spot. The spatial resolution of the spot in the lateral direction, which can be approximated by the spot radius when aggregation is not applied, will degrade to the root sum square of the spot radius and aggregation parameter. In treatment plans for the PMMA phantom, even though the mean value of the spot radius is approximately 7 mm, aggregation with a 7 mm parameter (σ) will degrade the spatial resolution to 9.9 mm. In the longitudinal direction, the spatial resolution will also be degraded by the uncertainty in the gap between the planned ranges of the aggregation and the neighboring spot sharing the same beam position. The uncertainty in the gap can be approximated by multiplying the length of the gap by the range uncertainty sourced from dose calculation (standard deviation: 3.1% when conservatively evaluated without Monte Carlo simulations [2]). For the aforementioned treatment plans, when aggregation with a 7 mm parameter (σ) is applied, the uncertainty in the gap is 0.22 mm ($\sigma \times 3.1\%$), and the maximum error in the gap is 0.65 mm ($3\sigma \times 3.1\%$). The aggregation parameters of 4, 7, and 10 mm were considered in the present study. The aggregation was performed for all spots and, then the ranges of the spots were measured by applying the range estimation algorithm [33] to the merged PG distributions.

In the present study, the error in range measurement was evaluated as the difference between the measured range and the true range. The true range was established based on the commissioning data in water, under the assumption that the PMMA's relative linear stopping power is a known constant of 1.16 [37]. This approach effectively minimized uncertainties associated with dose calculation, including those originating from CT imaging, calibration, conversion, and range degradation. Consequently, the uncertainty in true range primarily stemmed from sources independent of dose calculation, such as uncertainties in beam commissioning, compensator design, beam reproducibility, and patient setup, and is estimated to be approximately 0.8 mm (1.5 standard deviations) [2]. Further verification of the true range was conducted using dosimetry films (Gafchromic EBT3, Ashland, NJ) for three different energies (99.68, 130.42, and 159.78 MeV) [38], resulting in an error of less than 0.5 mm.

3. Results

3.1. Comparison with previous prototype

Fig. 4 plots the mean PG distribution obtained from the new and previous MSPGC prototypes, irradiating a solid phantom with a 95.09 MeV energy proton beam (with 8.73×10^9 protons per beam) for 100 repetitions. To enable a fair comparison, the mean PG distribution unit was set to counts per millimeter, rather than per slit, given that the two prototypes have different slit pitches. It is worth noting that the new prototype offers a field of view (FOV) measuring 216 mm, which is 1.5 times larger than that of the previous prototype (144 mm).

The results indicate that the new prototype offers 2.8 times higher PG detection efficiency than the previous prototype, based on the peak count (642 and 226 for the new and previous prototypes, respectively) [36]. Moreover, the SNR [36] of the new prototype (0.91) is 1.7 times higher than that of the previous prototype (0.54). Taking both PG detection efficiency and SNR into account, the FOM [36] of the new prototype is 4.8 times higher than that of the previous prototype (582 and 122, respectively).

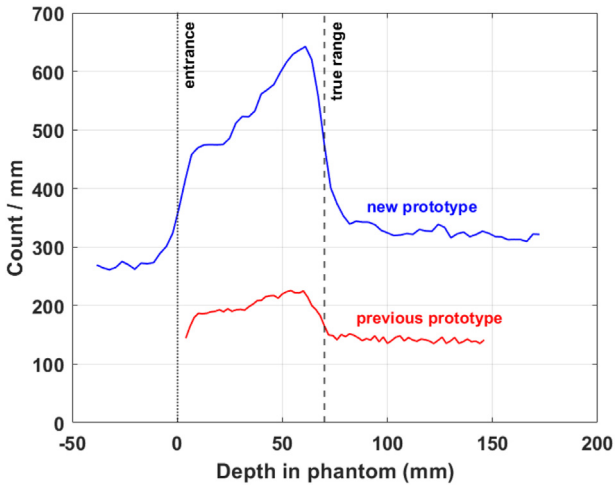

Fig. 4. Prompt-gamma distributions acquired by new and previous multi-slit prompt-gamma camera (MSPGC) prototypes.

3.2. Range measurement for single spot beam

3.2.1. Dependency on beam energy

Fig. 5 plots the beam ranges measured by the new MSPGC prototype when irradiating the PMMA phantom with proton beams of seven different energies (i.e., 99.68, 110.56, 119.22, 130.42, 140.69, 150.62, and 159.78 MeV, corresponding to true ranges of 62.2, 80.6, 92.2, 108.4, 123.6, 138.8, and 153.6 mm in the phantom, respectively). The measurements were repeated ten times for each beam energy, using a large number of protons (5×10^9 per spot beam) to minimize statistical fluctuations. The results indicate that the measured ranges are in excellent agreement with the true ranges, with mean errors less than 0.4 mm (less than 0.3% of the true range) across the wide range of beam energy. This shows that the new MSPGC prototype measures beam range accurately, regardless of

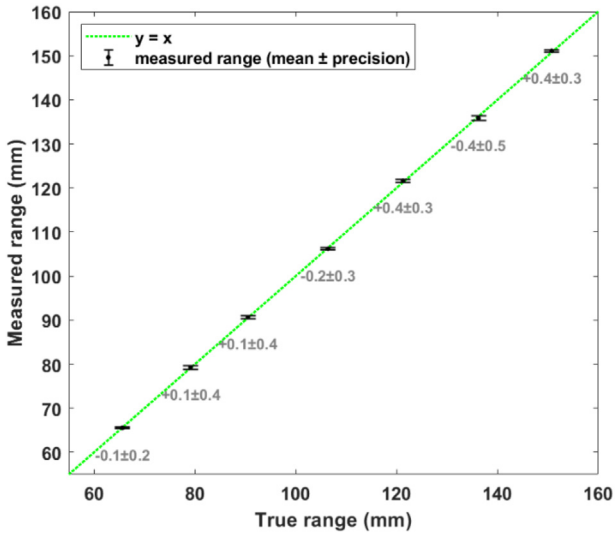

Fig. 5. Range of spot beam (unit: mm) for seven different energies measured by new multi-slit prompt-gamma camera (MSPGC) prototype. The black dots with error bars show the mean of measured range and precision in range measurement. The value below each error bar shows the mean error (i.e., the difference between the mean of the measured range and the true range) and precision in measurement. The green-dotted line indicates the ideal line (measured range = true range). (For interpretation of the references to colour in this figure legend, the reader is referred to the Web version of this article.)

the beam energy. The high precision in the range measurement (0.2–0.5 mm) is attributable to the large number of protons per spot.

3.2.2. Dependency on number of protons

Fig. 6a plots the range measurement precision of the new MSPGC prototype, in millimeter units, for eight different proton quantities (i.e., 2×10^7, 5×10^7, 1×10^8, 2×10^8, 5×10^8, 1×10^9, 2×10^9, and 5×10^9) and three beam energies (i.e., 99.68, 130.42, and 159.78 MeV) considered in the present study. Note that the ranges of spot beams were measured 100 times for each case to evaluate the precision in range measurement. The results show that the precision of the measurement tends to improve with the number of protons (i.e., 3 mm for 1×10^8 to 1 mm for 5×10^8 protons for 130.42 MeV) and that the precision tends to deteriorate with beam energy (i.e., from approximately 2.2 mm for 99.68 MeV to 3.7 mm for 159.78 MeV, for 1×10^8 protons). The decrease in precision was mainly attributed to the increase in background signal with beam energy, which blurs the distal edge in PG distribution [33]. Fig. 6b displays the precision as the ratio of itself to the true beam range. Less significant differences in range measurement precision were observed for different beam energies, due to the fact that the differences in precision (on the millimeter-scale) were offset by the different beam ranges. The precision in range measurement significantly improved with the number of protons per beam, from 2.8% at 1×10^8 to 0.2% at 5×10^9 on average. The precision was higher than 1% when the number of protons was larger than 5×10^8.

3.2.3. Dependency on positions of camera and beam

Fig. 7 plots the PG distributions and ranges measured for spot beams (energy: 99.68 MeV) of three different beam distances (i.e., 50, 100, and 150 mm) and four different beam elevations (i.e., 0, 25, 50, and 75 mm). The number of protons per spot beam was 1×10^8. As shown in Fig. 7a, significant differences in PG detection efficiency in terms of peak count were observed according to the distance (i.e., 136.3, 85.1, and 55.4 peak counts for distances of 50, 100, and 150 mm, respectively). The maximum difference in PG detection efficiency was 60% when the 100 mm distance was regarded as the reference. An increase in range measurement precision with improved efficiency was observed for a closer distance. Fig. 7b displays the PG distributions and ranges measured for different beam elevations (84.3, 80.7, 75.1, and 65.7 peak counts for beam elevations of 0, 25, 50, and 75 mm, respectively). The maximum difference in PG detection efficiency was 22% when the 0 mm beam elevation was taken as the reference. In comparison with the results for the beam distance, the beam elevation induced less difference in PG detection efficiency and range measurement precision. In all of the cases, the mean errors were smaller than 0.4 mm, reflecting high accuracy in range measurement over different beam distances and beam elevations.

3.3. Range measurement for spot-scanning proton beam

Fig. 8 displays the range measurement error (i.e., measured range minus true range) of the new MSPGC prototype for all spot beams used in the treatment of a CTV in the PMMA phantom with prescription doses of 1 and 2 Gy, using different aggregation parameters: 0 (aggregation not applied), 4, 7, and 10 mm. Without aggregation, significant errors (>10 mm) were observed for a large number of spot beams in both prescription dose cases. However, when aggregation was applied, the errors were significantly reduced, following a trend of decreasing error with increasing aggregation parameter, albeit with degraded spatial resolution. Fig. 9 presents the same results in the form of a histogram. The mean error and precision were 0.6 ± 11.8 ($\sigma = 0$ mm), -0.4 ± 2.1 ($\sigma = 4$ mm), -0.4 ± 0.9 ($\sigma = 7$ mm), and -0.4 ± 0.5 ($\sigma = 10$ mm) mm for the 1 Gy prescription dose and 0.3 ± 10.9 ($\sigma = 0$ mm), -0.5 ± 1.7 ($\sigma = 4$ mm), -0.5 ± 0.8 ($\sigma = 7$ mm), and -0.5 ± 0.5 ($\sigma = 10$ mm) mm for the 2 Gy prescription dose. High precision of range measurement (<1 mm, which is approximately equivalent to < 1% of the true range) was achieved with aggregation parameters of 7 mm or larger. The beam ranges were underestimated by 0.4–0.5 mm on average for all aggregation-applied cases, which seems due to phantom or camera setup error during the experiment.

4. Discussion

The results of the present study demonstrate the high precision of the new prototype in range measurement (approximately 1% of beam range for 5×10^8 protons), resulting from the improved PG detection efficiency and the powerful range estimation algorithm. Additionally, the FOV of the new prototype was increased to

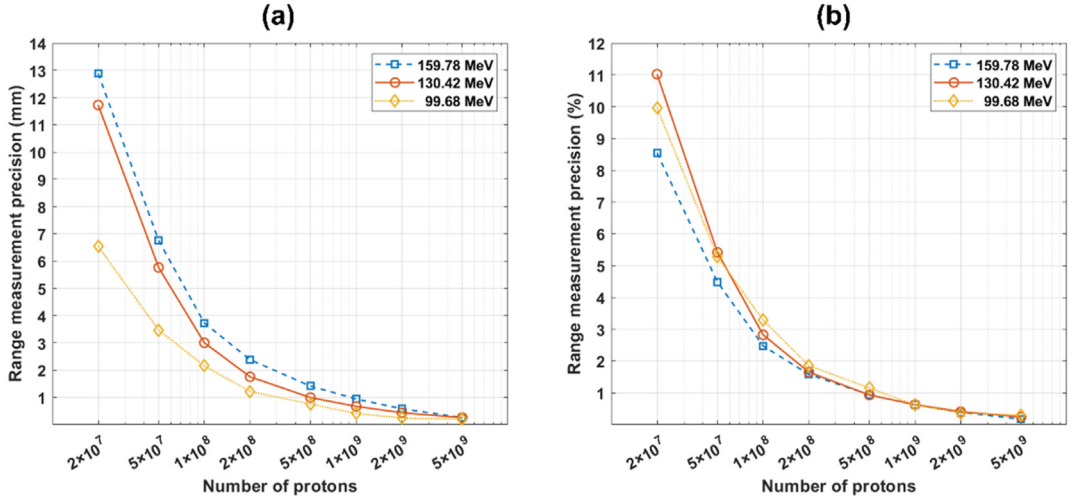

Fig. 6. Range measurement precision of multi-slit prompt-gamma camera (MSPGC) for spot beams of different proton quantities. The units for range measurement precision are (a) length in mm and (b) ratio (%) of itself to the beam range.

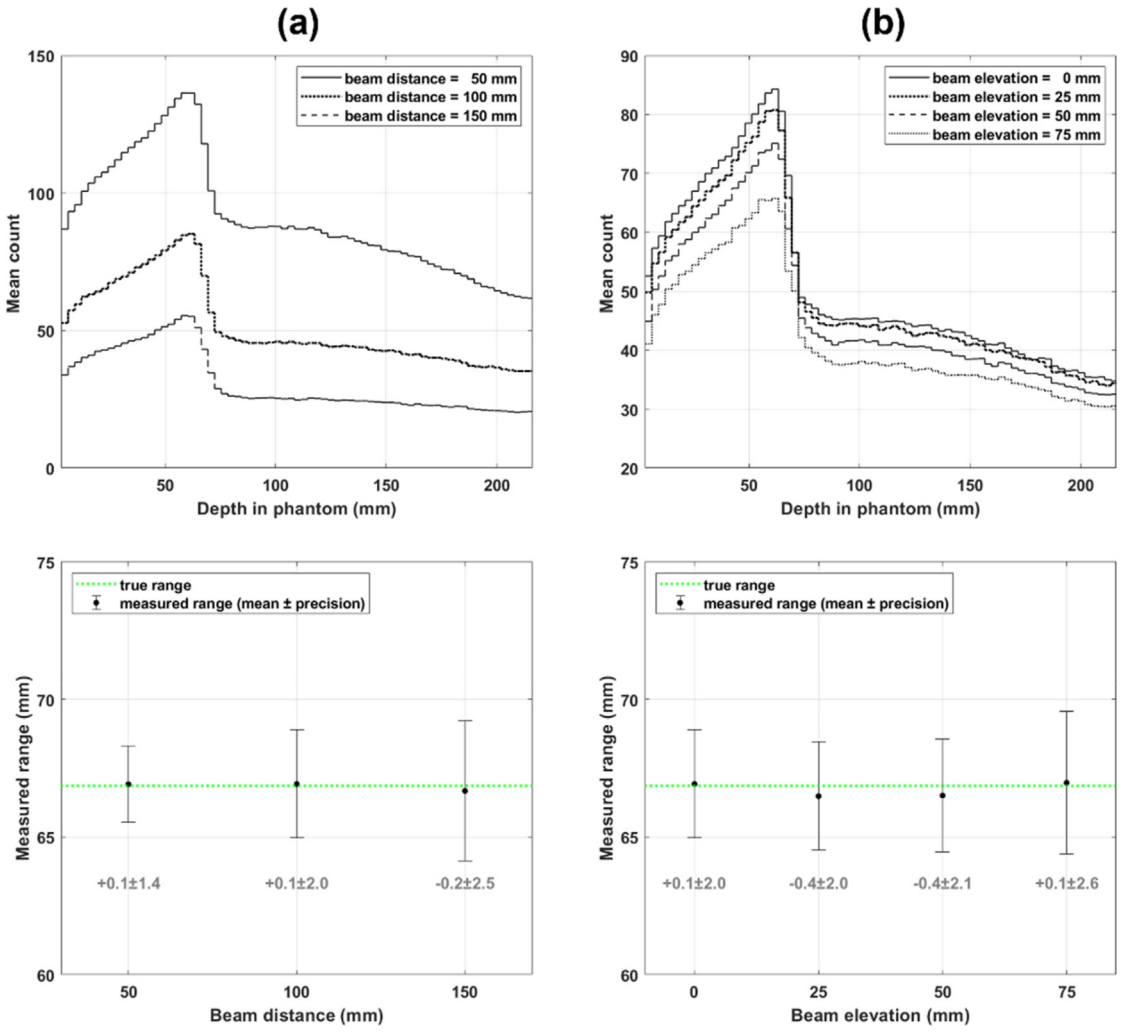

Fig. 7. Variation of prompt-gamma distributions and measured ranges for proton beams of 99.68 MeV as function of (a) beam distance and (b) beam elevation.

216 mm from the previous prototype's 144 mm. This large FOV of the new prototype will allow range measurement for all spots in a large treatment volume, such as the whole brain, with a single camera arrangement. This is a significant advantage over the knife-edge slit camera, which mostly monitors only the distal part of the treatment volume due to the limited FOV (100 mm in the typical setup [15]). Furthermore, considering that the entire falloff width in the PG distribution must be measured for range measurement, the effective FOV (i.e., FOV for range measurement) of the new prototype, which exhibits a sharper falloff in PG distribution, is significantly larger than that of the knife-edge slit camera. The effective FOV of the new prototype is approximately 195 mm (216 mm FOV − 21 mm falloff width; see Figs. 4 and 7), which is more than three times larger than that of the knife-edge camera (approximately 60 mm = 100 mm FOV − 40 mm falloff width) in the typical setup (see Fig. 2 in [15]).

The range measurement results for single spot beams showed that the PG detection efficiency and range measurement precision were more affected by beam distance than by beam elevation. This means that when measuring beam ranges, it is crucial to position the camera head as close to the beam path as possible. Close positioning of the camera head can be achieved by the automatic and precision positioning system developed in the present study. The developed positioning system still has a limitation: that is, when the beam nozzle occupies the floor (i.e., the gantry angle is near 180°), the camera head is difficult to position close to the clinical target. This limitation can be overcome by fixing the camera to the gantry using a robotic arm. The difference induced by the beam distance in PG detection efficiency and range measurement also suggests that using two MSPGCs facing each other is desirable, as this will double PG detection efficiency and compensate for the beam distance effect.

Currently, the range uncertainty in proton therapy is approximately 4% of the beam range [9], as the safety margins vary from 2.5% + 1.5 mm to 3.5% + 3 mm [2,41], depending on the hospitals. The range measurement precision of the new prototype, in the current study, was better than 4% when the number of protons was 1×10^8 (= typical number of protons for spots in distal layers) or larger. Furthermore, the precision reached approximately 2% and even 1% when the number of protons was 2×10^8 and 5×10^8, respectively. Fig. 10 shows a histogram of the number of protons per spot in the SSPT plan for the CTV used in the present study (i.e., applied aggregation parameter: 0 [aggregation not applied], 4, 7, and 10 mm; prescription dose: 1 Gy). Note that the number of protons was multiplied by the weight in aggregation. When aggregation was not applied, the number of protons per spot was

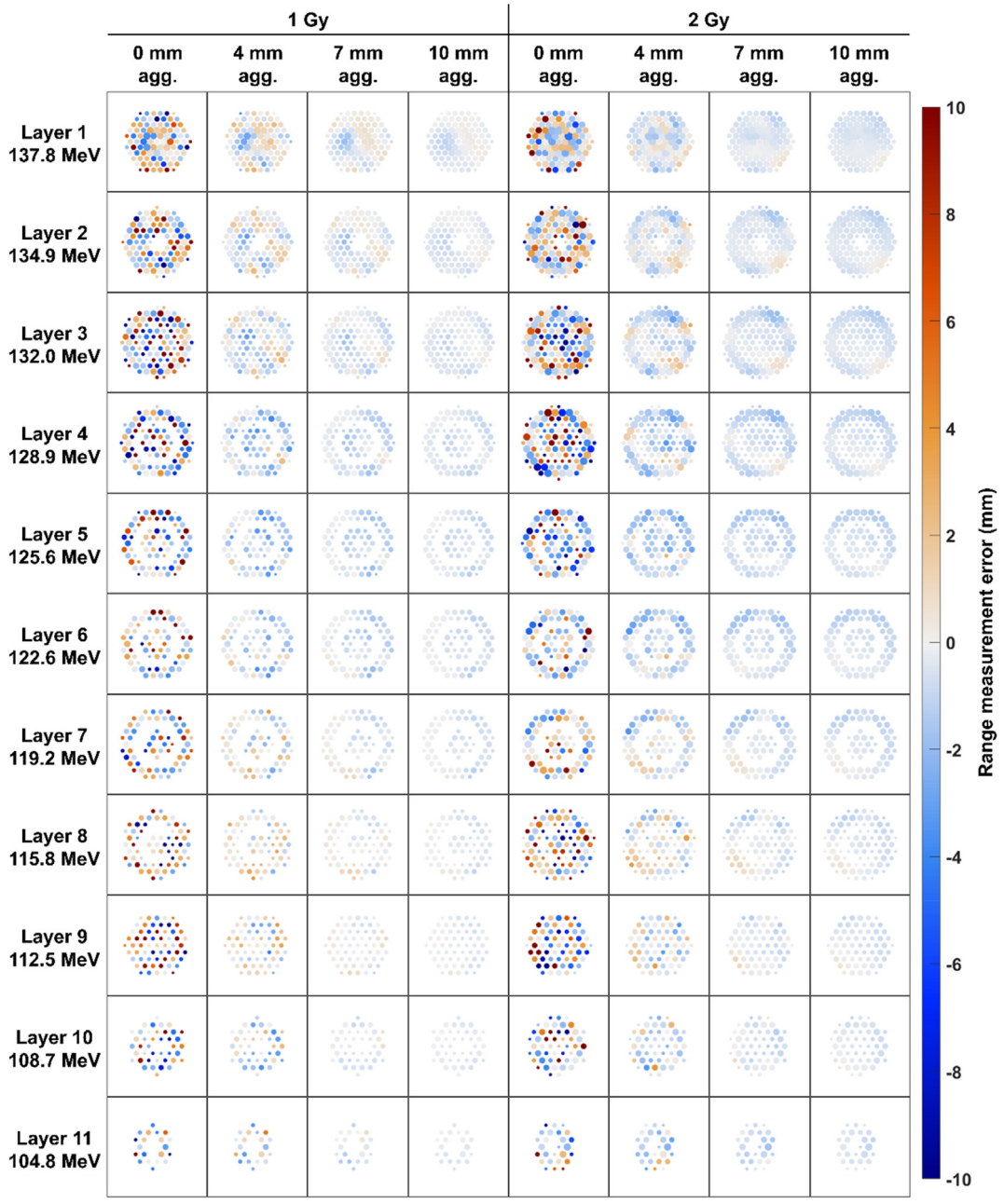

Fig. 8. Spot maps displaying range measurement error of each spot, as analyzed by applying different aggregation parameters when CTV was treated by SSPT with 1 and 2 Gy prescription doses. The spot size (area) is proportional to the number of protons.

smaller than 1.3×10^8, resulting in relatively low precision (11.8 mm) in range measurement. With a 7 mm or larger aggregation parameter, however, the number of protons per spot was larger than 7×10^8, showing high range measurement precision (<1 mm, equivalent to < 1% of the true range). These results show that range verification with the new MSPGC prototype can reduce range uncertainty in proton therapy with a proper degree of aggregation.

The treatment plans considered in the present study were formulated assuming conventional proton therapy (i.e., a 60 Gy total prescription dose in 30 fractions). On the other hand, in hypofractionated proton therapy or stereotactic body proton therapy, where a smaller number of fractions is applied compared to conventional proton therapy, the dose per fraction will be much higher, leading to higher counting statistics and higher precision in range measurement.

There are some limitations to the present study. Only homogeneous phantoms were considered in evaluating the intrinsic performance of the new prototype; that is, the influences of the heterogeneity of phantoms on PG distribution and range measurement were not considered. To fully evaluate clinical efficacy, the performance of the prototype needs to be tested with heterogeneous media, as patient anatomy is heterogeneous. In the near future, therefore, the performance of the new prototype will be evaluated with anthropomorphic phantoms and then with real patients.

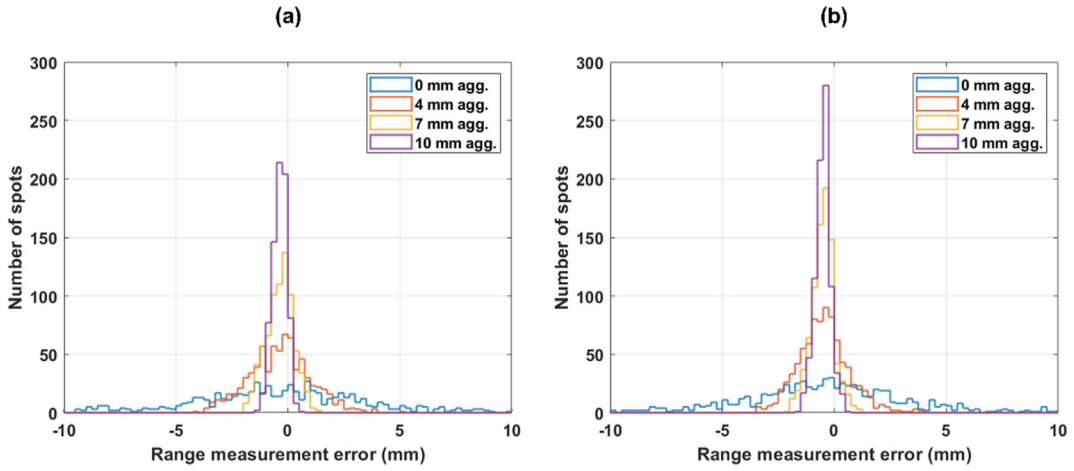

Fig. 9. Histograms of range measurement errors, as analyzed by applying different aggregation parameters when CTV was treated by SSPT with (a) 1 Gy and (2) 2 Gy prescription doses. The bin width in the histograms is 0.25 mm.

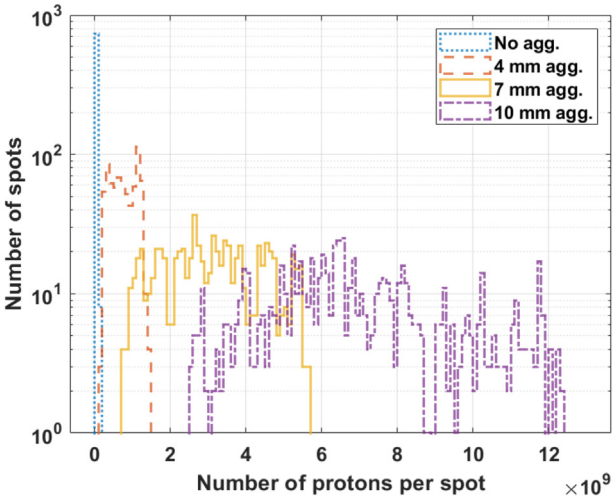

Fig. 10. Histogram of number of protons per spot without aggregation and with 4, 7, and 10 mm aggregation in SSPT plan (1 Gy) for CTV. The bin width in the histograms is 1×10^8.

5. Conclusion

In this study, we developed a new multi-slit prompt-gamma camera (MSPGC) prototype for clinical application in spot-scanning proton therapy (SSPT). This new prototype overcomes the limitations of its predecessor by enhancing prompt-gamma detection sensitivity, employing an advanced range estimation algorithm, and incorporating a precise camera positioning system. We evaluated the range measurement precision of the prototype for single spot proton beams with varying energies, proton quantities, and positions, as well as for spot-scanning proton beams planned for a PMMA phantom following a typical treatment procedure. Our results demonstrated high accuracy (<0.4 mm) in range measurement across the tested beam energies and positions. Measurement precision significantly increased with the number of protons, and the new prototype achieved 1% precision in range measurement with 5×10^8 or more protons. For spot-scanning proton beams, the prototype ensured more than 5×10^8 protons per spot with a 7 mm or larger spot aggregation, easily achieving 1% range measurement precision. Based on these findings, we anticipate that the clinical application of the new prototype will reduce range uncertainty (currently approximately 4%) to 1% or less. In the near future, we will evaluate the performance of this prototype under clinical conditions with heterogeneous media, such as anthropomorphic phantoms and real patients.

Declaration of competing interest

The authors declare that they have no known competing financial interests or personal relationships that could have appeared to influence the work reported in this paper.

Acknowledgments

This research was supported by the National Cancer Center Grants (NCC-2110390-3), Korea. Additionally, it received support from the National Research Foundation of Korea (NRF) grant funded by the Korea government (MSIT) (NRF-2019M2D2A1A02059814). The study was also backed by Field-oriented Technology Development Project for Customs Administration through National Research Foundation of Korea (NRF) funded by the Ministry of Science & ICT and Korea Customs Service (NRF-2021M3I1A1097895). Lastly, the National Research Foundation of Korea (NRF) grant, funded by the Korea government (Ministry of Science and ICT) (RS-2022-00144350), contributed to the research.

References

[1] R.R. Wilson, Radiological use of fast protons, Radiology 47 (1946) 487–491, https://doi.org/10.1148/47.5.487.
[2] H. Paganetti, Range uncertainties in proton therapy and the role of Monte Carlo simulations, Phys. Med. Biol. 57 (2012), https://doi.org/10.1088/0031-9155/57/11/R99.
[3] A. Fredriksson, R. Bokrantz, A critical evaluation of worst case optimization methods for robust intensity-modulated proton therapy planning, Med. Phys. 41 (2014), https://doi.org/10.1118/1.4883837.
[4] D. Pflugfelder, J.J. Wilkens, U. Oelfke, Worst case optimization: a method to account for uncertainties in the optimization of intensity modulated proton therapy, Phys. Med. Biol. 53 (2008) 1689–1700, https://doi.org/10.1088/0031-9155/53/6/013.
[5] J. Unkelbach, M. Alber, M. Bangert, R. Bokrantz, T.C.Y. Chan, J.O. Deasy, A. Fredriksson, B.L. Gorissen, M. Van Herk, W. Liu, H. Mahmoudzadeh, O. Nohadani, J.V. Siebers, M. Witte, H. Xu, Robust radiotherapy planning, Phys. Med. Biol. 63 (2018), https://doi.org/10.1088/1361-6560/aae659.
[6] J. Unkelbach, T. Bortfeld, B.C. Martin, M. Soukup, Reducing the sensitivity of IMPT treatment plans to setup errors and range uncertainties via probabilistic treatment planning, Med. Phys. 36 (2009) 149–163, https://doi.org/10.1118/1.3021139.
[7] W. Liu, X. Zhang, Y. Li, R. Mohan, Robust optimization of intensity modulated

proton therapy, Med. Phys. 39 (2012) 1079–1091, https://doi.org/10.1118/1.3679340.
[8] A.C. Knopf, A. Lomax, In vivo proton range verification: a review, Phys. Med. Biol. 58 (2013) 131–160, https://doi.org/10.1088/0031-9155/58/15/R131.
[9] S. Tattenberg, T.M. Madden, B.L. Gorissen, T. Bortfeld, K. Parodi, J. Verburg, Proton range uncertainty reduction benefits for skull base tumors in terms of normal tissue complication probability (NTCP) and healthy tissue doses, Med. Phys. (2021), https://doi.org/10.1002/mp.15097.
[10] J. Krimmer, D. Dauvergne, J.M. Létang, Testa, Prompt-gamma monitoring in hadrontherapy: a review, Nucl. Instruments Methods Phys. Res. Sect. A Accel. Spectrometers, Detect. Assoc. Equip. 878 (2018) 58–73, https://doi.org/10.1016/j.nima.2017.07.063.
[11] F. Stichelbaut, Y. Jongen, Verification of the proton beam position in the patient by the detection of prompt gamma rays emission, in: 39th Meet. Part, San Fr., 2003, pp. 1–5. Ther. Co-Op. Gr.
[12] C.H. Min, C.H. Kim, M.Y. Youn, J.W. Kim, Prompt gamma measurements for locating the dose falloff region in the proton therapy, Appl. Phys. Lett. 89 (2006) 2–5, https://doi.org/10.1063/1.2378561.
[13] M. Moteabbed, S. España, H. Paganetti, Monte Carlo patient study on the comparison of prompt gamma and PET imaging for range verification in proton therapy, Phys. Med. Biol. 56 (2011) 1063–1082, https://doi.org/10.1088/0031-9155/56/4/012.
[14] L. Nenoff, M. Priegnitz, G. Janssens, J. Petzoldt, P. Wohlfahrt, A. Trezza, J. Smeets, G. Pausch, C. Richter, Sensitivity of a prompt-gamma slit-camera to detect range shifts for proton treatment verification, Radiother. Oncol. 125 (2017) 534–540, https://doi.org/10.1016/j.radonc.2017.10.013.
[15] Y. Xie, E.H. Bentefour, G. Janssens, J. Smeets, F. Vander Stappen, L. Hotoiu, L. Yin, D. Dolney, S. Avery, F. O'Grady, D. Prieels, J. McDonough, T.D. Solberg, R.A. Lustig, A. Lin, B.K.K. Teo, Prompt gamma imaging for in vivo range verification of pencil beam scanning proton therapy, Int. J. Radiat. Oncol. Biol. Phys. 99 (2017) 210–218, https://doi.org/10.1016/j.ijrobp.2017.04.027.
[16] M. Priegnitz, S. Barczyk, L. Nenoff, C. Golnik, I. Keitz, T. Werner, S. Mein, J. Smeets, F. Vander Stappen, G. Janssens, L. Hotoiu, F. Fiedler, D. Prieels, W. Enghardt, G. Pausch, C. Richter, Towards clinical application: prompt gamma imaging of passively scattered proton fields with a knife-edge slit camera, Phys. Med. Biol. 61 (2016) 7881–7905, https://doi.org/10.1088/0031-9155/61/22/7881.
[17] J.H. Park, S.H. Kim, Y. Ku, C.H. Kim, H.R. Lee, J.H. Jeong, S.B. Lee, D.H. Shin, Multi-slit prompt-gamma camera for locating of distal dose falloff in proton therapy, Nucl. Eng. Technol. 51 (2019) 1406–1416, https://doi.org/10.1016/j.net.2019.03.008.
[18] S.H. Kim, J.H. Jeong, Y. Ku, J. Jung, C.H. Kim, Performance prediction of gamma electron vertex imaging (GEVI) system for interfractional range shift detection in spot scanning proton therapy, Nucl. Eng. Technol. 54 (2021) 2213–2220, https://doi.org/10.1016/j.net.2021.12.027.
[19] C. Hyeong Kim, J. Hyung Park, H. Seo, H. Rim Lee, Gamma electron vertex imaging and application to beam range verification in proton therapy, Med. Phys. 39 (2012) 1001–1005, https://doi.org/10.1118/1.3662890.
[20] H.R. Lee, S.H. Kim, J.H. Park, W.G. Jung, H. Lim, C.H. Kim, Prototype system for proton beam range measurement based on gamma electron vertex imaging, Nucl. Instruments Methods Phys. Res. Sect. A Accel. Spectrometers, Detect. Assoc. Equip. 857 (2017) 82–97, https://doi.org/10.1016/j.nima.2017.03.022.
[21] S.H. Kim, J.H. Jeong, Y. Ku, J. Jung, S. Cho, K. Jo, C.H. Kim, Upgrade of gamma electron vertex imaging system for high-performance range verification in pencil beam scanning proton therapy, Nucl. Eng. Technol. (2021), https://doi.org/10.1016/j.net.2021.09.001.
[22] C.H. Kim, H.R. Lee, S.H. Kim, J.H. Park, S. Cho, W.G. Jung, Gamma electron vertex imaging for in-vivo beam-range measurement in proton therapy: experimental results, Appl, Phys. Lett. 113 (2018), https://doi.org/10.1063/1.5039448.
[23] F. Roellinghoff, M.H. Richard, M. Chevallier, J. Constanzo, D. Dauvergne, N. Freud, P. Henriquet, F. Le Foulher, J.M. Létang, G. Montarou, C. Ray, E. Testa, M. Testa, A.H. Walenta, Design of a Compton camera for 3D prompt-γ imaging during ion beam therapy, Nucl. Instruments Methods Phys. Res. Sect. A Accel. Spectrometers, Detect. Assoc. Equip. 648 (2011) 87–94, https://doi.org/10.1016/j.nima.2011.01.069.
[24] M. Frandes, A. Zoglauer, V. Maxim, R. Prost, A tracking compton-scattering imaging system for hadron therapy monitoring, IEEE Trans. Nucl. Sci. 57 (2010) 144–150, https://doi.org/10.1109/TNS.2009.2031679.
[25] J.C. Polf, S. Avery, D.S. Mackin, S. Beddar, Imaging of prompt gamma rays emitted during delivery of clinical proton beams with a Compton camera: feasibility studies for range verification, Phys. Med. Biol. 60 (2015) 7085–7099, https://doi.org/10.1088/0031-9155/60/18/7085.
[26] J. Krimmer, J.L. Ley, C. Abellan, J.P. Cachemiche, L. Caponetto, X. Chen, M. Dahoumane, D. Dauvergne, N. Freud, B. Joly, D. Lambert, L. Lestand, J.M. Létang, M. Magne, H. Mathez, V. Maxim, G. Montarou, C. Morel, M. Pinto, C. Ray, V. Reithinger, E. Testa, Y. Zoccarato, Development of a Compton camera for medical applications based on silicon strip and scintillation detectors, Nucl. Instruments Methods Phys. Res. Sect. A Accel. Spectrometers, Detect. Assoc. Equip. 787 (2015) 98–101, https://doi.org/10.1016/j.nima.2014.11.042.
[27] D. MacKin, S. Peterson, S. Beddar, J. Polf, Evaluation of a stochastic reconstruction algorithm for use in Compton camera imaging and beam range verification from secondary gamma emission during proton therapy, Phys. Med. Biol. 57 (2012) 3537–3553, https://doi.org/10.1088/0031-9155/57/11/3537.
[28] E. Draeger, D. Mackin, S. Peterson, H. Chen, S. Avery, S. Beddar, J.C. Polf, 3D prompt gamma imaging for proton beam range verification, Phys. Med. Biol. 63 (2018), https://doi.org/10.1088/1361-6560/aaa203.
[29] C. Richter, G. Pausch, S. Barczyk, M. Priegnitz, I. Keitz, J. Thiele, J. Smeets, F. Vander Stappen, L. Bombelli, C. Fiorini, L. Hotoiu, I. Perali, D. Prieels, W. Enghardt, M. Baumann, First clinical application of a prompt gamma based in vivo proton range verification system, Radiother. Oncol. 118 (2016) 232–237, https://doi.org/10.1016/j.radonc.2016.01.004.
[30] J.H. Park, S.H. Kim, Y. Ku, H.S. Lee, C.H. Kim, D.H. Shin, J.H. Jeong, Comparison of knife-edge and multi-slit camera for proton beam range verification by Monte Carlo simulation, Nucl. Eng. Technol. 51 (2019) 533–538, https://doi.org/10.1016/j.net.2018.10.002.
[31] J. Petzoldt, G. Janssens, L. Nenoff, C. Richter, J. Smeets, Correction of geometrical effects of a knife-edge slit camera for prompt gamma-based range verification in proton therapy, Instruments 2 (2018) 25, https://doi.org/10.3390/instruments2040025.
[32] Y. Xing, B. Macq, Improvement of Bragg peak shift estimation using dimensionality reduction techniques and predictive linear modeling, 18, https://doi.org/10.1117/12.2285608, 2017.
[33] Y. Ku, J. Jung, C.H. Kim, New algorithm to estimate proton beam range for multi-slit prompt-gamma camera, Nucl. Eng. Technol. 54 (2022) 3422–3428, https://doi.org/10.1016/j.net.2022.04.019.
[34] D.A. Gedcke, W.J. McDonald, A constant fraction of pulse height trigger for optimum time resolution, Nucl. Instrum. Methods 55 (1967) 377–380, https://doi.org/10.1016/0029-554X(67)90145-0.
[35] C.H. Min, H.R. Lee, C.H. Kim, S.B. Lee, Development of array-type prompt gamma measurement system for in vivo range verification in proton therapy, Med. Phys. 39 (2012) 2100–2107, https://doi.org/10.1118/1.3694098.
[36] H.J. Choi, J.W. Jang, W.G. Shin, H. Park, S. Incerti, C.H. Min, Development of integrated prompt gamma imaging and positron emission tomography system for in vivo 3-D dose verification: a Monte Carlo study, Phys. Med. Biol. 65 (2020), https://doi.org/10.1088/1361-6560/ab857c.
[37] R. Zhang, W.D. Newhauser, Calculation of water equivalent thickness of materials of arbitrary density, elemental composition and thickness in proton beam irradiation, Phys. Med. Biol. 54 (2009) 1383–1395, https://doi.org/10.1088/0031-9155/54/6/001.
[38] L. Zhao, I.J. Das, Gafchromic EBT film dosimetry in proton beams, Phys. Med. Biol. 55 (2010), https://doi.org/10.1088/0031-9155/55/10/N04.
[39] F. Hueso-González, M. Rabe, T.A. Ruggieri, T. Bortfeld, J.M. Verburg, A full-scale clinical prototype for proton range verification using prompt gamma-ray spectroscopy, Phys. Med. Biol. 63 (2018), https://doi.org/10.1088/1361-6560/aad513.
[40] S.H. Kim, J.H. Park, Y. Ku, H.S. Lee, Y. Kim, C.H. Kim, J.H. Jeong, Improvement of statistics in proton beam range measurement by merging prompt gamma distributions: a preliminary study, J. Radiat. Prot. Res. 44 (2019) 1–7, https://doi.org/10.14407/jrpr.2019.44.1.1.
[41] C. Hahn, J. Eulitz, N. Peters, P. Wohlfahrt, W. Enghardt, C. Richter, A. Lühr, Impact of range uncertainty on clinical distributions of linear energy transfer and biological effectiveness in proton therapy, Med. Phys. 47 (2020) 6151–6162, https://doi.org/10.1002/mp.14560.